N-Cyanoimine as an electron-withdrawing functional group for organic semiconductors: example of dihydroindacenodithiophene positional isomers

Jean-David Peltier, Benoît Heinrich, Bertrand Donnio, Olivier Jeannin, Joëlle Rault-Berthelot, Emmanuel Jacques, Cyril Poriel

N-cyanoimine as electron-withdrawing functional group for Organic Semiconductors: Example of Dihydroindacenodithiophene positional isomers

Jean-David Peltier,[a] Benoît Heinrich,[c] Bertrand Donnio,[c] Olivier Jeannin,[a] Joëlle Rault-Berthelot,[a*] Emmanuel Jacques[b*] Cyril Poriel[a*]

Manipulating the frontier molecular orbitals by chemical design is one of the chief aspect in organic electronics. For an application in the field of n-type organic field-effect transistors (OFET), depressing the LUMO energy level is particularly important to ensure efficient charge injection. In this work, we report the incorporation of electron-withdrawing cyanoimine functional groups on the bridges of dihydroindacenodithiophene regioisomers. Cyanoimines are barely known in the field of organic electronics but herein have been found to be highly efficient to depress the LUMO energy level of an organic semiconductor and can thus be envisaged as an attractive alternative to widely known electron-withdrawing units such as dicyanovinylene. This work focusses on a detailed structure-property relationship study, including incorporation in n-type OFETs, of two dihydroindacenodithiophene regioisomers bearing two cyanoimine groups either in a *syn*- or an *anti*-configuration. As far as we know, this work is only the second example reported to date on N-cyanoimines incorporated in n-type OFETs and shows the potential of these functional groups in organic electronics.

Introduction

In the last decades, the development of organic electronics has increased the demand of new organic semiconductors (OSCs) adapted to their use in specific devices such as organic light-emitting diodes (OLED)[1, 2] using either fluorescent[3-5] or phosphorescent[6-9] emitting materials, organic photovoltaics (OPV)[10-12] or organic field-effect transistors (OFET).[13-17] The fantastic development of this technology has been possible thanks to a strong synergy between physics and chemistry. The chemists have notably synthesized highly efficient OSCs which are the heart of the devices. The molecular construction of an OSC is often based on the association of a π-conjugated fragment on which are attached functional groups to tune electronic/physical properties in order to fit with a precise device. Among the numerous OSCs designed, those based on bridged oligoarylenes and especially on "bridged ter-arylene" such as dihydroindenofluorenyl (IF) or dihydroindacenodithienyl (IDT) derivatives have been the subject of intense researches due to the high versatility of such extended cores. Indeed, IF- and IDT-based materials have found applications in the four main organic devices: OLED,[18-22] PhOLED,[7, 23-25] OPV[26-30] and OFETs.[31-37] The easy modulation of the electronic/physical properties of IF and IDT cores is at the origin of this versatility. Three main design techniques are generally used to tune their properties: (i) modification of the geometry by positional isomerism, (ii) substitution of the constituting aryl units, and (iii) bridges functionalization.

Positional isomerism is surely the most original design strategy used in recent years to manipulate the properties of bridged oligoarylenes.[19, 21, 22, 34, 38-45] It consists in modifying the linkages (to modify the electronic coupling between the three constituting aryl units) and/or the ring bridges arrangements (to modify the geometry of the molecules). Indeno[1,2-*b*]fluorene-6,12-dione **1,2-*b*-IF(=O)$_2$**[46] (framed in green in chart 1) and s-indaceno[1,2-*b*:5,6-*b'*]dithiophene-4,9-dione ***para*-IDT(=O)$_2$**[34, 39] (framed in green in chart 2) are the so-called *para-anti* isomers built on the association of three phenyl units in **1,2-*b*-IF(=O)$_2$** or one phenyl unit and two thienyl units in *para*-IDT(=O)$_2$. These units are connected by a *para* linkage and the two ketone bridges are in an *anti*-configuration. Both platforms have been widely studied in the last fifteen years and will be discussed below. Their corresponding *meta-syn* isomers indeno[2,1-*b*]fluoren-10,11-dione **(2,1-*b*-IF(=O)$_2$)**[37] and s-indaceno[1,2-*b*:7,6-*b'*]dithiophene-4,6-dione **(*meta*-IDT(=O)$_2$)**[34, 39] are the second generation of positional isomers, possessing a *meta*-linkage and a *syn*-configuration of the bridges (charts 1 and 2). Thanks to the low LUMO energy levels of these four platforms, many efficient electron-poor materials for n-type OFETs, the main topic of this work, have been constructed. However, *para-syn* isomers **1,2-*b*-IF(=O)$_2$** and ***para*-IDT(=O)$_2$** have been far more studied than *meta-syn* isomers **2,1-*b*-IF(=O)$_2$** and ***meta*-IDT(=O)$_2$**, see below.

[a] Univ Rennes, CNRS, ISCR-UMR CNRS 6226, F-35000 Rennes, France.
[b] Univ Rennes, CNRS, IETR-UMR CNRS 6164, F-35000 Rennes, France.
[c] Institut de Physique et Chimie des Matériaux de Strasbourg (IPCMS), UMR 7504, CNRS-Université de Strasbourg, 23 rue du Loess, BP 43, 67034 Strasbourg Cedex 2, France.

Electronic Supplementary Information (ESI) available: [details of any supplementary information available should be included here]. See DOI: 10.1039/x0xx00000x

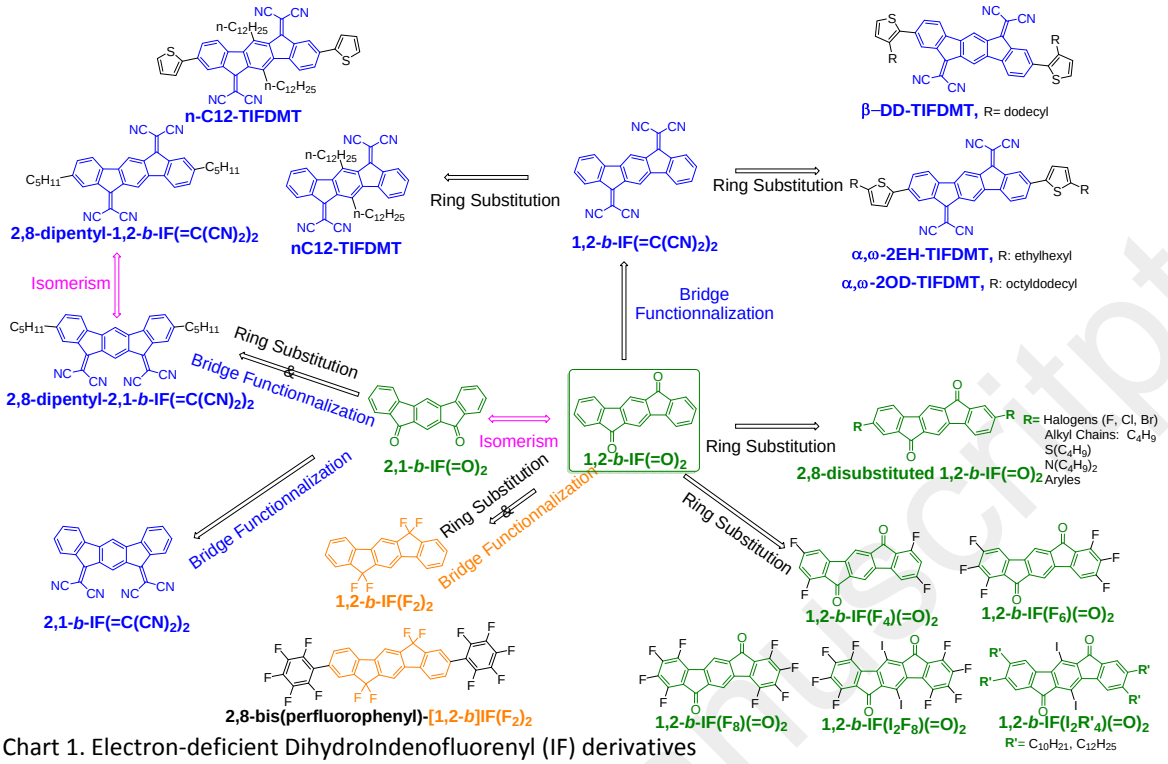

Chart 1. Electron-deficient DihydroIndenofluorenyl (IF) derivatives

The second design strategy is the classical substitution of the three constituting aryl units. In the IF-dione series, the disubstitution of the side phenyl rings of **1,2-*b*-IF(=O)$_2$** has widely been studied whereas it is almost absent for its regioisomer **2,1-*b*-IF(=O)$_2$**.[23, 37, 47-50] Alkyl chains,[51] amines,[51] halogen atoms[32, 52] or substituted thiophenes[53, 54] have been for example introduced in **1,2-*b*-IF(=O)$_2$**. Recently, Zhan et al have notably reported an **1,2-*b*-IF(=O)$_2$** based material possessing S-butyl side chains at C2 and C7 positions displaying an ambipolar character with very high hole and electron mobility μ_{FE} (0.71 and 0.65 cm^2 V^{-1} s^{-1} resp.).[51] Poly-substitutions of the side phenyl units **(1,2-*b*-IF(F$_4$)(=O)$_2$**,[32] **1,2-*b*-IF(F$_6$)(=O)$_2$**,[32, 55] **1,2-*b*-IF(F$_8$)(=O)$_2$**[56]) or of all the phenyl units **(1,2-*b*-IF(I$_2$)(F$_8$)(=O)$_2$**,[56] **1,2-*b*-IF(I$_2$)(C$_{12}$H$_{25}$)$_4$(=O)$_2$**[57] or **1,2-*b*-IF(I$_2$)(C$_{10}$H$_{21}$)$_4$(=O)$_2$**[57]) have also been described, leading in some cases to highly efficient materials with low LUMO energy level and high μ_{FE} such as in **1,2-*b*-IF(F$_6$)(=O)$_2$** (LUMO= -3.53 eV, μ_E= 0.16 cm^2 V^{-1} s^{-1}).[32]

Similarly, ***para*-IDT(=O)$_2$**[58, 59] (framed in green chart 2) or from its isomer ***meta*-IDT(=O)$_2$**, (which synthesis has not been reported so far) have followed similar design strategies.[34, 39] Disubstitution at C2 and C7 of ***para*-IDT(=O)$_2$** has been performed for example with ethyl,[60] hexyl[34, 60-62] or dodecyl[60] groups. If changing the alkyl groups has a weak impact on the electronic properties of the OSCs, the corresponding OFETs can exhibit drastically different transport characteristics such as shown by Zhang and co-workers. Indeed, electron mobilities decrease from 0.22 cm^2 V^{-1} s^{-1} for ***para*-IDT(2,7-didodecyl)(=O)$_2$** to 0.03 cm^2 V^{-1} s^{-1} for ***para*-IDT(2,7-diethyl)(=O)$_2$**[60] and to 0 cm^2 V^{-1} s^{-1} for ***para*-IDT(2,7-dihexyl)(=O)$_2$** showing the chief role played by the side chains on the device performance.

Alternatively, hexyl groups were also positioned at C3 and C8 of the IDT core (***para*-IDT(3,8-dihexyl)(=O)$_2$**) in order to allow additional substitutions of the central core for example with alkyl chains (***para*-IDT(2,3,7,8-tetrahexyl)(=O)$_2$**) or with thienyl units (***para*-IDT(3,8-dihexyl)(2,7-dithienyl)(=O)$_2$** or ***para*-IDT(3,8-dihexyl)(2,7-dioligothienyl)(=O)$_2$**).[63] Introduction of thienyl pending units allows to strongly decrease the oxidation potentials from 0.72 V for ***para*-IDT(3,8-dihexyl)(=O)$_2$** to 0.36 V for ***para*-IDT(3,8-dihexyl)(2,7-terthienyl)(=O)$_2$** due to the extension of the conjugation.[63] A similar strategy was also employed for **DDPP-PhCO** by introduction of two diketopyrrolopyrrole-thienyl fragments (chart 2).[33]

As for IF series presented above, *meta* isomer ***meta*-IDT(=O)$_2$** has been far less explored than *para* isomer and only 2,8-dihexyl-s-indaceno[1,2-b:7,6-b']dithiophene-4,6-dione(***meta*-IDT(2,8-dihexyl)-(=O)$_2$**) has been reported.[34]

The last strategy consists in modifying the bridges. Thanks to the ketone borne by the bridges, **1,2-*b*-IF(=O)$_2$** and ***para*-IDT(=O)$_2$** (or their alkyl substituted analogues) are versatile platforms to introduce other functional groups at the bridges. Difluoromethylene bridges[64, 65] in **1,2-*b*-IF(F$_2$)$_2$** derivatives (in orange chart 1) have for example been investigated but the most studied chemical modification to generate electron-poor materials is the incorporation of a dicyanovinylene unit[54, 66] (see different substituted **1,2-*b*-IF(=C(CN)$_2$)$_2$** and ***para*-IDT(=C(CN)$_2$)$_2$** coloured in blue in charts 1 and 2). The electron-withdrawing effect of dicyanovinylene bridges induces a strong lowering of the LUMO energy level (by more than 0.6 eV) compared to their corresponding diones **1,2-*b*-IF(=O)$_2$ /*para*-IDT(=O)$_2$**.[34, 37] Often, this LUMO levels lowering leads to an important increase of the OFETs performance notably in term of electron mobility.[66, 67] For example, ***para*-IDT(=C(CN)$_2$)$_2$** displays interesting characteristics in n-channel OFET (μ_{FE} = 7.1 × 10^{-2} cm^2 V^{-1} s^{-1}, I_{Don}/I_{Doff} of 2.3 × 10^7 and subthreshold swing of 1.2 V/dec)[34] whereas its corresponding dione ***para***-

IDT(=O)$_2$ not. Similarly, **2,1-*b*-IF(=C(CN)$_2$)$_2$**[31, 37] and ***meta*-IDT(=C(CN)$_2$)$_2$**[34] with their low LUMO level (-3.81 and -4.07 eV resp.) have been successfully used in n-channel OFETs and even incorporated in "pseudo-complementary metal oxide semiconductor" inverters.[37]

Following these design approaches, very efficient dicyanovinylene-IF-based compounds incorporating thienyl rings, have been synthesized by the groups of Marks, Fachetti and Usta (**nC12-TIFDMT**, **β-DD-TIFDMT**, **α,ω-2OD-TIFDMT**, **α,ω-2EH-TIFDMT**)[66, 68] reaching very high electron mobility (0.11 $cm^2\ V^{-1}\ s^{-1}$ for **α,ω-2OD-TIFDMT**[68] for example). These works have highlighted the importance of the position of the alkyl chains on the device performance.

However, in the field of OFETs, the molecular diversity of the electron-withdrawing groups incorporated on the bridges of dihydroindenofluorene or dihydroindacenodithiophene fragments is very limited and even almost exclusively based on dicyanovinylenes and ketones. In 1983, a N-cyanoimine group, which is the association of a nitrile group to a sp^2 nitrogen atom has been introduced on the bridges of a structurally related dihydroindeno[2,1-*a*]indene.[69] In 1984, the potential of this unit as electron acceptor was envisaged.[70] However, only few examples have been reported to date (cyclohexadienes,[70] dihydroanthracene,[71, 72] spiro[5,5]undecatetraene[73] benzodifuran[74] or benzodithienyl).[74-76] As far as we know, no precise structure-properties-device performance relationship study on this interesting functional group has been done and only one example of OFET is reported using thiophene-fused dicyanoquinonediimine.[76] The electronic and physical effects of N-cyanoimines on the bridges of π-conjugated systems are therefore rarely reported.

The present work will focus on this feature and aim at exploiting the lack of efficient functional groups used to depress the LUMO energy level of bridged OSCs. We provide herein a detailed structure-properties-device performance relationship study including synthesis, physicochemical properties (electrochemistry, absorption spectroscopy, powder and single crystal X-ray diffraction, differential scanning calorimetry), molecular modelling (DFT and TD-DFT) and incorporation in n-type OFETs (using SU-8 as insulator and with self-assembled monolayer of 4-(dimethylamino)benzene thiol) of two IDT regioisomers possessing N-cyanoimines on the bridges namely ***para*-IDT(=NCN)$_2$** and ***meta*-IDT(=NCN)$_2$** (framed in red chart 2). In these examples, we notably show that N-cyanoimines display interesting packing characteristic, are thermally stable, and as efficient as dicyanovinylenes to depress the LUMO energy level of bridged OSCs and can be successfully introduced as active layer in n-type OFETs with low subthreshold swing.

Results and discussion

Synthetic procedures

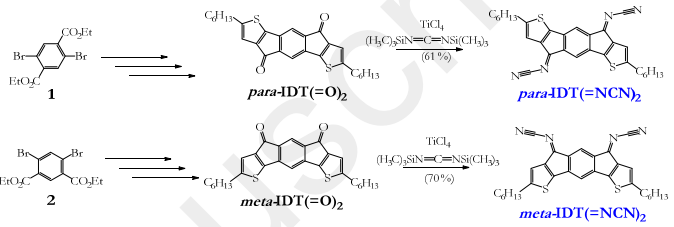

Scheme 1 Synthesis of ***para*-IDT(=NCN)$_2$** (top) and ***meta*-IDT(=NCN)$_2$** (bottom).

In materials science, a key feature for chemists consists in synthesizing target OSCs in a short and highly efficient manner and if possible by using common synthetic intermediates. Herein, ***para*-IDT(=NCN)$_2$** and ***meta*-IDT(=NCN)$_2$** were obtained from their corresponding diones ***para*-IDT(=O)$_2$** and ***meta*-IDT(=O)$_2$** synthesized at the gram scale from diester **1** or **2** as previously reported.[34] These diones are also central building blocks in the synthesis of dicyanovinylene analogues ***para*-IDT(=C(CN)$_2$)$_2$** and ***meta*-IDT(=C(CN)$_2$)$_2$**.[34] Thus, non-enolizing diones ***para*-IDT(=O)$_2$** and ***meta*-**

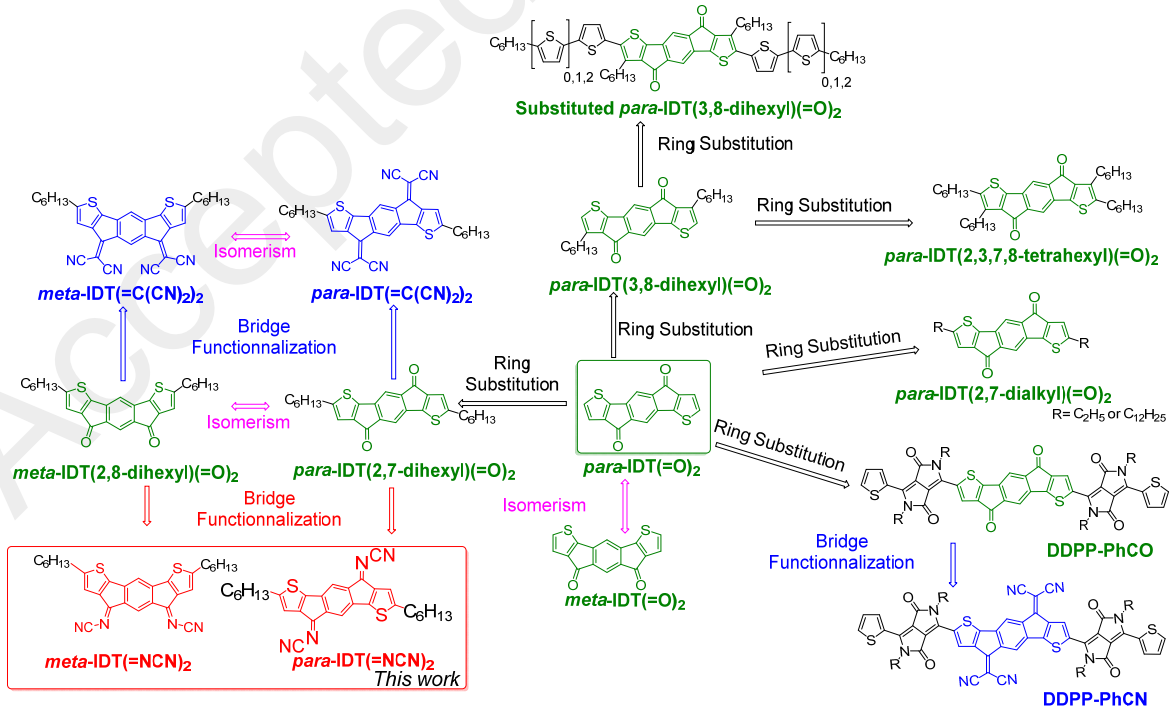

Chart 2. Electron-deficient indacenodithienyl (IDT) derivatives

IDT(=O)$_2$ react with N,N-bis-(trimethylsilyl)carbodiimide in the presence of titanium tetrachloride[70-72, 76] to provide target ***para*-IDT(=NCN)$_2$** and ***meta*-IDT(=NCN)$_2$** as green-brown powders with good yields of 61 and 70 % respectively (

Scheme 1). These syntheses are short (4 steps), easy to perform and possess good overall yields of 20% and 32% for ***para*-IDT(=NCN)$_2$** and ***meta*-IDT(=NCN)$_2$** respectively.

It is important to note that both compounds were more soluble in common organic solvents than their dicyanovinylene analogues ***para*-IDT(=C(CN)$_2$)$_2$** and ***meta*-IDT(=C(CN)$_2$)$_2$**.[34] These compounds will be used herein as model compounds to evaluate the impact of the cyanoimine group on the properties.

Molecular conformation and self-assembling

Single crystals of ***para*-IDT(=NCN)$_2$** and ***meta*-IDT(=NCN)$_2$** were obtained from chloroform/methanol mixture (Figs. 1-5).

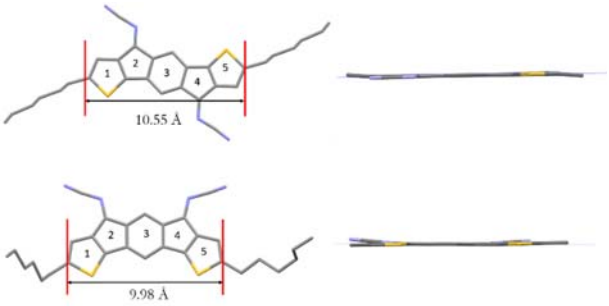

Fig. 1 Molecular structures from X-ray crystallography of ***para*-IDT(=NCN)$_2$** (top) and ***meta*- IDT(=NCN)$_2$** (bottom).

***Para*-IDT(=NCN)$_2$** crystallized in the P-1 space group with one molecule per asymmetric unit (Fig. 1, top). The central *para*-substituted IDT core (rings 1 to 5) has a length of 10.55 Å similar to those previously reported in literature for structurally related compounds.[39, 77] Due to the *para* linkage, the central *para*-substituted IDT core is almost flat with small dihedral angles of 0.15° between the two mean planes of the thienyl rings 1 and 5 and that of the central phenyl 3 (a distance of 0.026 Å between the two mean planes of the thienyl units, which are parallel, is measured). The distance between the two nitrogen atoms of the N-cyanoimine groups and the mean plane of the *para*-IDT core are for both measured at 0.03 Å for the nitrogen atom of the imine group and at 0.06 Å for the nitrogen atom of the cyano group showing that the cyanoimine groups are nearly in the mean plane of the *para*-IDT core. The planarity of the *para*-IDT core in ***para*-IDT(=NCN)$_2$** is even more marked than that observed for identical *para*-IDT cores possessing different bridge functionalization. For a *para*-IDT core substituted on the bridges with tolyl units,[77] Wong and coworkers have indeed reported an angle of 2.68° between the two mean planes of the thienyl units and that of the central phenyl ring. Our groups have shown that *para*-IDT core may even be more deformed with rigid spiro-connected fluorene units in the bridges(angle of 3.39°).[39] This shows that the bridges can modify the planarity of the IDT cores by packing forces and/or intramolecular interactions. It should indeed be mentioned that cyano of the cyanoimine groups exclusively point toward the sides of the molecules due to intramolecular "short contacts" (corresponding to an interatomic distance inferior to the sum of the Van der Waals radii of the involved atoms) between the carbon atom of the cyano units and the carbon and hydrogen atoms in β position of the thienyl rings (Fig. 2, top). No intramolecular interaction is observed between the *para*-IDT core and the hexyl chains.

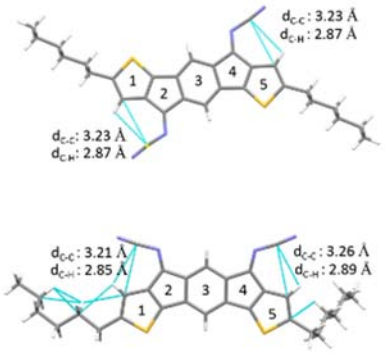

Fig.2 Intramolecular short-contacts in ***para*-IDT(=NCN)$_2$** (top) and in ***meta*- IDT(=NCN)$_2$** (bottom).

***Meta*-IDT(=NCN)$_2$** also crystallized in the P-1 space group with one molecule by asymmetric unit (Fig. 1, bottom). The central *meta*-IDT core of ***meta*-IDT(=NCN)$_2$** (rings 1-5) has a length of 9.98 Å, which is shorter than that of ***para*-IDT(=NCN)$_2$** (10.55 Å) due to the different linkage (*para* vs *meta*) of the central phenyl ring. A similar influence of the linkages has been previously shown with other bridged π-conjugated systems such as dihydroindenofluorenes.[22, 24, 25]

As observed for its *para* isomer, ***meta*-IDT(=NCN)$_2$** is almost planar with very weak angles between the plane of phenyl ring 3 and those of each thienyl ring 1 and 5 (1.2 and 2° *resp.*). Note these angles are nevertheless higher than that measured for ***para*-IDT(=NCN)$_2$** (0.15°, see above). Another deformation is observed in ***meta*-IDT(=NCN)$_2$** with an angle of 3.41° detected between the mean plane of thienyl ring 1 and thienyl ring 5. This feature differs to what is observed in ***para*-IDT(=NCN)$_2$** were the two thienyl rings are in two parallel planes.

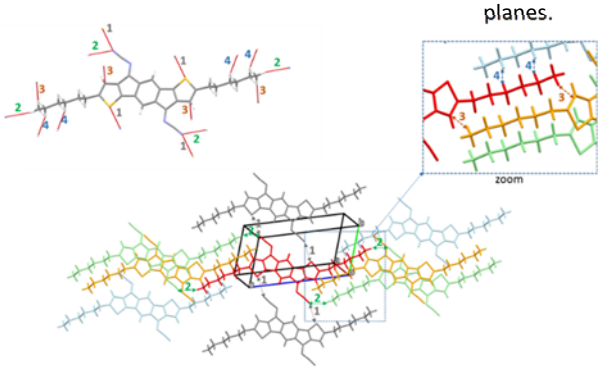

Fig. 3 Intermolecular interactions in ***para*-IDT(=NCN)$_2$**.

The distances between the two nitrogen atoms of the imine groups and the mean plane of the *meta*-IDT core are different for the two bridges (0.07 / 0.03 Å for the nitrogen atoms of the imine and 0.30 / 0.15 Å for the nitrogen atoms of the cyano groups). Thus, the imine groups are pointed out of the mean plane of the *meta*-IDT core on the same side of this plane and in opposite direction of the hexyl units. As for the *para* isomer, the terminal cyano groups point exclusively towards the sides of the molecule due to intramolecular interactions between the carbon atom of the cyano units and the carbon and hydrogen atoms in β position of the thienyl rings (Fig. 2,

bottom). Additionally, some intramolecular interactions are also observed between the *meta*-IDT core and its two hexyl chains that appear differently bent.

One of the most important features is linked to the different supramolecular organizations of the two isomers, ***para*-IDT(=NCN)$_2$** and ***meta*-IDT(=NCN)$_2$**, described below. These structural features can be assigned to the different geometry of the two cores and the resulting position of the two imines, in an *anti* (***para*-IDT(=NCN)$_2$**) or in a *syn* configuration (***meta*-IDT(=NCN)$_2$**).

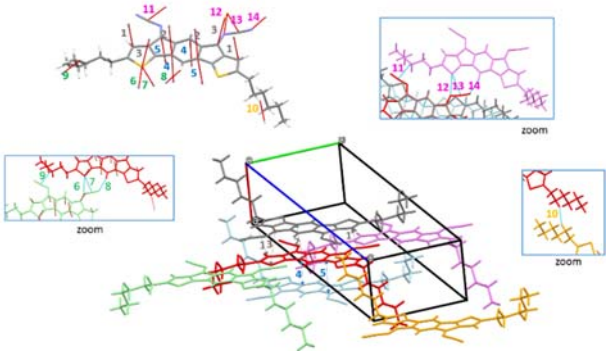

Fig. 4 Intermolecular interactions in ***meta*-IDT(=NCN)$_2$**.

Many intermolecular "short contacts" are detected in the packing diagram of both ***para*-IDT(=NCN)$_2$** (Fig. 3) and ***meta*-IDT(=NCN)$_2$** (Fig. 4). Interestingly, these intermolecular interactions appear to arise from different atoms for the two isomers, which explain the different packing diagrams discussed below. Some short contacts are particularly detected for the three atoms of the imine group clearly highlighting the importance of the bridge functionalities in the packing diagram. The exhaustive list of the short intermolecular distances is gathered in ESI.

One may additionally note that the inter-planar distance between two *para*-IDT cores and three stacked *meta*-IDT core are short: 3.41 Å in ***para*-IDT(=NCN)$_2$** and 3.36 or 3.37 Å in ***meta*-IDT(=NCN)$_2$** (Fig. 5). In the light of Janiak's works,[78] detailed in ESI, centroid-centroid distances, vertical displacements and ring slippage angles between cofacial thienyl and phenyl rings (rings 1/1', 2/2' and 3/3' for *para*-IDT and rings 1/1', 2/2' and 3/3' or rings 1'/1'', 2'/2'' and 3'/3'' for *meta*-IDT cores) have been measured clearly highlighting strong intermolecular interactions (see values in ESI).

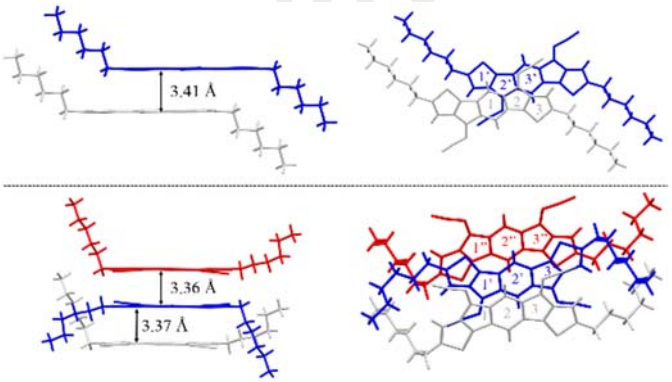

Fig. 5 Arrangement of two or three molecules in the packing diagram of ***para*-IDT(=NCN)$_2$** (top) and of ***meta*-IDT(=NCN)$_2$** (bottom).

Molecular self-organization in the crystalline and mesomorphic states

Thermal behaviour. The two isomers were investigated by thermogravimetric analysis (TGA), differential scanning calorimetry (DSC) and small- and wide-angle X-ray scattering (S/WAXS). Both compounds start to degrade above 250 °C and possess high 5% weight temperatures T_d (at around 364 and 365 °C respectively, for the *para*- and *meta*-isomer, see TGA traces in Electronic Supplementary Information (ESI) showing a high thermal stability of both compounds, even slightly higher than the one of ***para*-** and ***meta*-IDT(=C(CN)$_2$)$_2$**[34] (T_d recorded around 349 and 352 °C resp.). As thermal stability is a key feature for Organic Electronics, TGA traces show that N-cyanoimine groups are appealing from this point of view.

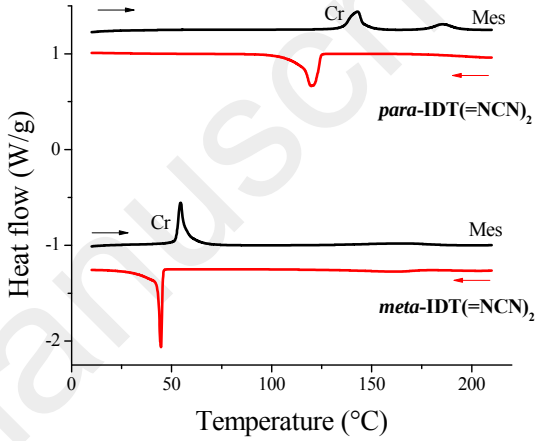

Fig. 6. DSC traces of IDT(=NCN)$_2$ regioisomers (1st heating run (black) and cooling run (red) at 5°C/min, endotherm up); Cr: crystalline phase; Mes: meso phase.

As observed in DSC traces at the first heating curves presented in Fig. 6 (see the second heating curves in ESI), ***para*-IDT(=NCN)$_2$** melts at 139 °C (ΔH = 25 J/g), far above its isomer ***meta*-IDT(=NCN)$_2$** (52°C, ΔH = 28 J/g) which indicates stronger cohesion of its crystalline self-organization. As a matter of fact, both compounds exhibit even lower melting temperatures than their diketone or dicyanovinylene analogues (around 170 °C for ***para*-IDT(=O)$_2$** and ***para*-IDT(=C(CN)$_2$)$_2$**[34]; around 145 °C for ***meta*-IDT(=O)$_2$** and ***meta*-IDT(=C(CN)$_2$)$_2$**)[34] whereas cyanoimine groups like dicyanovinylenes, give rise to strong molecular association through dipolar interactions. This feature indeed explains that the positional long-range order persists for **IDT(=NCN)$_2$** and **IDT(=C(CN)$_2$)$_2$** derivatives above the melting temperature, within broad mesomorphic ranges extending to above 250°C. **IDT(=O)$_2$** derivatives in contrast do not give rise to such strong dipolar association and directly melt to the isotropic liquid phase. The early melting of the crystalline structures of **IDT(=NCN)$_2$** derivatives is therefore not a matter of molecular association strength, but likely of sterically constrained crystalline self-assembling.

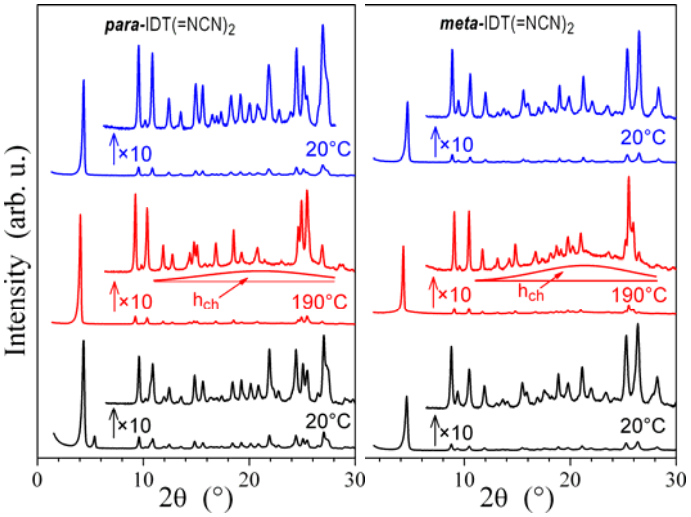

Fig. 7 S/WAXS patterns of ***para*-IDT(=NCN)$_2$** (left) and ***meta*-IDT(=NCN)$_2$** (right) at room temperature in the pristine state (bottom, black), at 190 °C (middle, red) and then at room temperature after cooling (top, blue) ; h_{ch} is the scattering signal from molten alkyl chains.

Molecular self-organization. The self-organization of both **IDT(=NCN)$_2$** regioisomers was investigated by S/WAXS in crystalline and mesomorphic states (Fig. 7). Similarly to the previously reported **IDT(=C(CN)$_2$)$_2$**,[34] all states consist in lamellar structures, defined by the alternation of layers of conjugated cores and aliphatic tails (Fig. 8). While the previous derivatives only crystallize into fine powdered solids unsuitable for single-crystal investigation, the single-crystal structures obtained for **IDT(=NCN)$_2$** gives access to the detailed molecular self-assembling within lamellae and to the three dimensional structure formed by the superposition of lamellae.

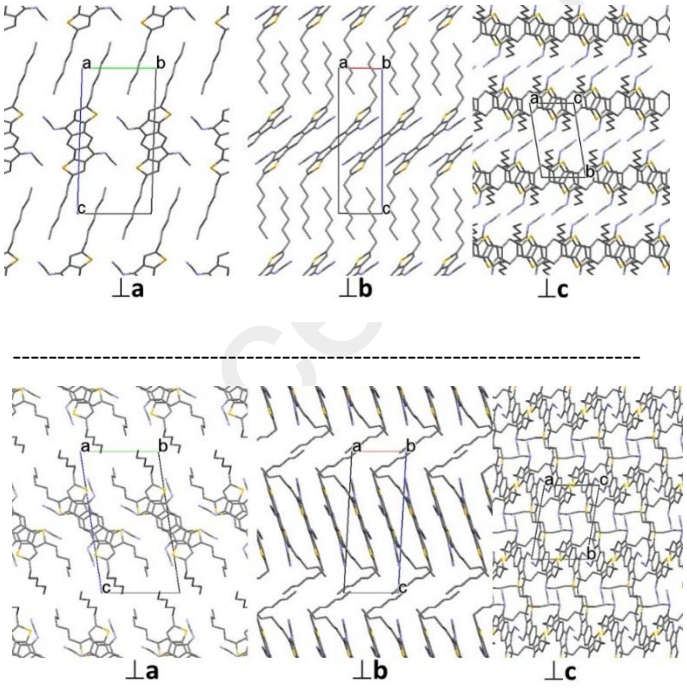

Fig. 8 Views of the crystal structure of ***para*-** and ***meta*-IDT(=NCN)$_2$** (top-bottom).

In both isomeric structures, the core layers present a ribbon substructure emerging from the π-stacking of the lath-like fused-rings into columns that alternate with parallel strips of =NCN groups, self-associated with dipolar interactions. The π-stacking distances perpendicular to the ring planes (h_π = 3.25-3.3 Å) are moreover similar, leading to equivalent compactness (***para*-IDT(=NCN)$_2$**: ρ = 1.305 g/cm^3; ***meta*-IDT(=NCN)$_2$**: ρ = 1.298 g/cm^3). Yet, the arrangements in the lamellar plane are different, due to connection of =NCN groups on either both sides or identical side of the rigid core. Their connection on opposite sides in the para configuration authorizes unique core orientation and arrangement in a single-molecule a×b sublattice. In the *meta* configuration, the unsymmetrically substituted cores have to revert their orientation in the sublattice plane to allow their compact association into dipolar strips. This implies sublattice and thus cell doubling, which in this particular structure occurs in the direction of the rows of π-stacked molecules, through their alternated lateral orientation. As a result, substituents are equally distributed on both sides of rows and are engaged in symmetrical dipolar strips, maintaining the structure periodicity to a single row. In addition, if the dipolar association induces comparably large tilt angles of cores within layers in both structures (ψ = 44-45° for para; ψ = 40-41° for meta), the directions of tilt in the layer plane are turned for the two row configurations. The *para* IDT cores are tilted in the stacking direction (i.e. along *a*-axis), presumably because tilting in another direction would impact negatively on the dipolar association, as each molecule is engaged in two strips through the antiparallel alignment of the =NCN groups. The constraints on the tilt direction are released for the *meta* isomer, so that a different direction is effectively observed, affecting the area projected on the lamellar plane (stacking and ribbon periodicities for *para*: h_{stack} = 4.896, d_{rib} = 8.824 Å; for *meta*: h_{stack} = 3.457, d_{rib} = 9.827 Å). Finally, it should be mentioned that the molecular area A_{mol}, ratio of molecular volume V_{mol} and periodicity *d*, of ***para*-IDT(=NCN)$_2$** (A_{mol} = 40.29 Å^2; $\sigma_c = A_{mol}\times\cos(\psi)$ = 28-29 Å^2) exceeds the section of ca. 2×18.5 Å^2 for two crystallized chains[79] and that a compact intercalated monolayer of chains is effectively formed in this case, whereas this threshold is not reached for the *meta* isomer ***meta*-IDT(=NCN)$_2$** (A_{mol} = 34.90 Å^2; σ_c = 26-27 Å^2) and chains accordingly arrange in strongly tilted double-layers (Table 1).[80]

Table 1 Structural parameters of the triclinic structures adopted by ***meta*-** and ***para*-IDT(NCN)$_2$** in the single crystal state at -123°C, in the crude powder at 20°C and in the mesophase at 190°C, whereas indexation of the room temperature pattern of *para*-isomer failed, presumably due to coexistence of several modifications: *a*, *b*, *c*, α, β, γ, *V*, *Z* and ρ are the parameters, volume, number of molecules per cell and density of the triclinic lattices; d_{001} and Z_L are the cell periodicity along the sequence of molecular layers and the number of involved layers; A and Z_A are the area of the sublattice formed by the lateral arrangement of molecules and the number of involved molecules.

Compound Temperature [°C]	Lattice parameters [Å, °]	Lattice volume [Å^3] Density [g/cm^3]	Periodicity ⊥a×b [Å] In-plane area a×b [Å^2]
***meta*-IDT(=NCN)$_2$** T = -123	*a* = 7.0293; *b* = 10.0818; *c* = 8.972(3) α = 81.078; β = 85.448; γ = 80.052	*V* = 1306.4 (*Z* = 2) ρ = 1.2984	d_{001} = 18.716 (Z_L = 1) A = 69.80 (Z_A = 2)
***para*-IDT(=NCN)$_2$** T = -123	*a* = 4.8961; *b* = 8.3385; *c* = 16.1441 α = 91.827; β = 90.314; γ = 99.320	*V* = 650.0 (*Z* = 1) ρ = 1.305	d_{001} = 16.135 (Z_L = 1) A = 40.29 (Z_A = 1)
***meta*-IDT(=NCN)$_2$** T = 20	*a* = 7.20(4); *b* = 10.22(0); *c* = 9.15(2) α = 81.6(7); β = 85.9(0); γ = 79.2(6)	*V* = 1369 (*Z* = 2) ρ = 1.239	d_{001} = 18.93 (Z_L = 1) A = 72.3 (Z_A = 2)
***meta*-IDT(=NCN)$_2$** T = 190	*a* = 7.42(0); *b* = 10.05(0); *c* = 41.9(7) α = 82.5(2); β = 84.7(8); γ = 77.5(6)	*V* = 3023 (*Z* = 4) ρ = 1.122	d_{001} = 41.6 (Z_L = 2) A = 72.7 (Z_A = 2)
***para*-IDT(=NCN)$_2$** T = 190	*a* = 7.34(3); *b* = 9.85(4); *c* = 43.9(6) α = 84.8(8); β = 83.9(6); γ = 76.7(4)	*V* = 3072 (*Z* = 4) ρ = 1.104	d_{001} = 43.7 (Z_L = 2) A = 70.3 (Z_A = 2)

Indexation of the room temperature S/WAXS patterns performed in the crystalline powder state of ***meta*-IDT(=NCN)$_2$** demonstrated the

same triclinic structure as in the single-crystal state, with only slight deviations of the lattice parameters due to thermal expansion (Table 1). The powder melts at low temperature to a pasty-like solid, identified to a mesophase with a high degree of positional order. The mesomorphic nature of this phase is indeed confirmed by the appearance in the S/WAXS patterns of the broad scattering signal h_{ch}, corresponding to the molten chains, while the numerous sharp reflections (Fig. 7) indicate that the IDT(=NCN)$_2$ cores remain organized in a long-range correlated three-dimensional cell, throughout the molten chains layers. The cell geometry turned out to be triclinic, with an *a*×*b* sublattice close to that of the crystalline powder. Impressively, there is almost no variation of A_{mol} between crystal and mesophase, suggesting that the internal structure of the core layers is hardly affected by the melting process (Table 2). The main alteration of the geometry, with respect to crystal, is an increase of the lamellar periodicity that follows the higher volume contribution of molten chains and the thermal expansion. The further structural change consists in the doubling of the lattice along *c*-axis, meaning that the cell now includes two laterally shifted lamellae. In contrast, the structure of ***para*-IDT(=NCN)$_2$** in the powder crystalline state is obviously very different from that of its single-crystal structure, as deduced from the composition of the room-temperature S/WAXS pattern. Indexation trials failed, possibly because of the coexistence of several crystalline states. On heating, the crystalline powder melts to a highly ordered triclinic mesophase similar to that of the *meta* isomer, with in particular the same numbers of lamellae per cell and of molecules per sublattice, and quite comparable lattice parameters. The main difference between both regioisomers comes down to slightly less expanded lamellae for the ***para*-**isomer in the mesomorphic state and on the contrary to more expanded lamellae in the crystalline state, in relation with the formation of an intercalated aliphatic layer. This configuration is expectedly less cohesive than the bilayer of strongly tilted chains of the ***meta*-**isomer, which is presumably one main cause for its lower melting temperature.

Table 2. Geometrical parameters of the self-organization of ***meta*-** and ***para*-IDT(=NCN)$_2$** in the single crystal state at -123°C, in the crude powder at 20°C and in the mesophase at 190°C, and comparison with ***meta*-** and ***para*-IDT(=C(CN)$_2$)$_2$**: d = d_{001}/Z_L is the periodicity of the lamellae formed the alternation of IDT and aliphatic layers, $V_{mol} = V/Z$ is the molecular volume (values for ***meta*-** and ***para*-IDT(=C(CN)$_2$)$_2$** are calculated using reference volume data), $A_{mol} = V_{mol}/d$ is the molecular area, i.e. the average area covered by a molecule in the plane of the layers.

	Structure type	T [°C]	d [Å]	V_{mol} [Å^3]	A_{mol} [Å^2]
***meta*-IDT(=NCN)$_2$**	Single crystal	-123	18.716	653.2	34.90
***para*-IDT(=NCN)$_2$**	Single crystal	-123	16.135	650.0	40.29
***meta*-IDT(=NCN)$_2$**	Powder	20	18.93	685	36.2
***meta*-IDT(=NCN)$_2$**	Mesophase	190	20.79	756	36.4
***para*-IDT(=NCN)$_2$**	Mesophase	190	21.86	768	35.1
***meta*-IDT(=C(CN)$_2$)$_2$**	Mesophase	190	23.13	792	34.2
***para*-IDT(=C(CN)$_2$)$_2$**	Mesophase	190	24.14	804	33.3

Finally, the use of cyanoimine groups instead of dicyanovinylene maintained the broad-range lamellar mesomorphism, with only a slightly higher lateral expansion of lamellae (Table 2). A major contribution to this higher A_{mol} is obviously the tilted directions of cyanoimine groups that induce the tilting of the whole core, whereas dicyanovinylene groups are essentially orthogonal to the core axis. Beyond these details, the self-organization of the four compounds appears thus rather comparable.

Electrochemical properties.

Electrochemical studies of the two isomers were performed in Bu_4NPF_6 0.2 M /CH_2Cl_2 solutions at a concentration of 10^{-3} M for ***meta*-IDT(=NCN)$_2$** and of 0.5 × 10^{-3} M for ***para*-IDT(=NCN)$_2$**. The cyclic voltammetries (CVs) are presented in Fig. 9. All the peak potentials obtained from the CVs are summarized in Table 3. Both compounds present similar CVs with two reversible reduction waves between 0.0 and -1.0 V and one weakly reversible oxidation wave with a maximum around 1.46 V for ***para*-IDT(=NCN)$_2$** and at 1.7 V for ***meta*-IDT(=NCN)$_2$**.

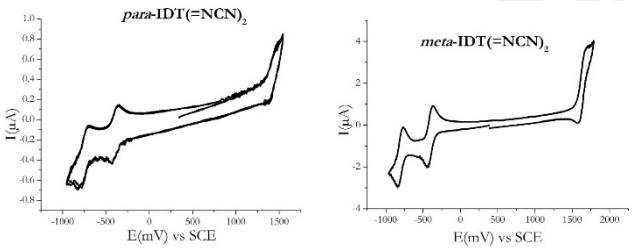

Fig. 9. CV of ***para*-IDT(=NCN)$_2$** (left) and ***meta*-IDT(=NCN)$_2$** (right) (10^{-3} M) recorded in CH_2Cl_2 + Bu_4NPF_6 0.2 M, sweep-rate 100 mV.s^{-1}. Platinum disk (Ø: 1mm) working electrode.

In oxidation, both compounds display an oxidation at higher potential values than those recorded for their structurally related analogues ***para*-** and ***meta*-IDT(=C(CN$_2$)$_2$)**[34] (Table 3). The onset oxidation potentials of the present cyanoimines based compounds are indeed shifted by 80 mV in the *para*-series (from 1.24 to 1.32 V) and by 160 mV in the *meta*-series (from 1.40 to 1.56 V) compared to their dicyanovinylene analogues. As this oxidation wave can be assigned to an electron transfer centred on the IDT core (see the electronic distribution of the HOMO, Fig. 10), the potential difference may be assigned to a stronger electron-withdrawing effect of the cyanoimine units compared to the dicyanovinylene units. Surprisingly, this effect does not significantly exist in reduction, as both isomers present a very similar onset reduction potential at ca -0.3 V (-0.27 V for ***para*-IDT(=NCN)$_2$**) and -0.33 V for ***meta*-IDT(=NCN)$_2$**). The electronic distribution of the LUMOs is identical for both isomers and centred on the two cyclopentadienyl-N-cyanoimine rings (Fig. 10). Since the side phenyl rings are not involved in the LUMO distribution, this feature explains why the onset reduction potentials are very similar for both isomers. From the onset oxidation and reduction potentials recorded at 1.32 and -0.27 V for ***para*-IDT(=NCN)$_2$** and at 1.56 and -0.33 V for ***meta*-IDT(=NCN)$_2$**, we determined the HOMO/LUMO energies of the two compounds at -5.72 / -4.13 eV for ***para*-IDT(=NCN)$_2$** and at -5.96 / -4.07 eV for ***meta*-IDT(=NCN)$_2$**. The LUMO are very deep (below -4 eV) and hence adapted to application in n-type OFETs (see below).

The difference between the HOMO energy levels of ***para*-** and ***meta*-IDT(=NCN)$_2$** is assigned to a disruption of the conjugation in the latter due to the *meta* connection between the phenyl and the thienyl rings and the resulting partial electronic decoupling (note that in the light of recent works, the π-conjugation is not completely interrupted by a *meta* linkage and has a different influence on singlet and triplet energies and on HOMO/LUMO energy levels [38]). Indeed, in the case

of ***meta*-IDT(=NCN)$_2$**, there is a conjugation breaking in the middle of the central phenyl of the *meta*-IDT core (see electronic distribution of the HOMO Fig. 10, bottom) leading to a deeper HOMO level compare to its *para* isomer (-5.96 vs -5.72 eV). The energy difference between the two HOMO levels (0.16 eV) is similar to that calculated for the two IDT-dicyanovinylene (0.17 eV) confirming that the IDT core is at the origin of this feature and not the bridge functionalization.

The electrochemical gaps of both ***para*-IDT(=NCN)$_2$** and ***meta*-IDT(=NCN)$_2$** are very short, 1.59 eV and 1.89 eV respectively and the difference between the two isomers is mainly assigned to the different HOMO energy (difference of 0.24 eV). In addition, one can note that the LUMO energies of ***para*-** and ***meta*-IDT(=NCN)$_2$** are very similar to those of ***para*-** and ***meta*-IDT(=C(CN$_2$)$_2$)**, indicating that the bridge functionalization by =C(CN)$_2$ or by =NCN leads to similar electronic effects on the LUMO energy. This is an important finding in this work, which shows the strong potential of cyanoimine groups to depress the LUMO level of a bridge ter-arylene. Thus, the gap of such bridged ter-arylene can be tuned either by positional isomerism (geometry) or by bridges functionalization, which both influence the HOMO energy without altering the LUMO energy.

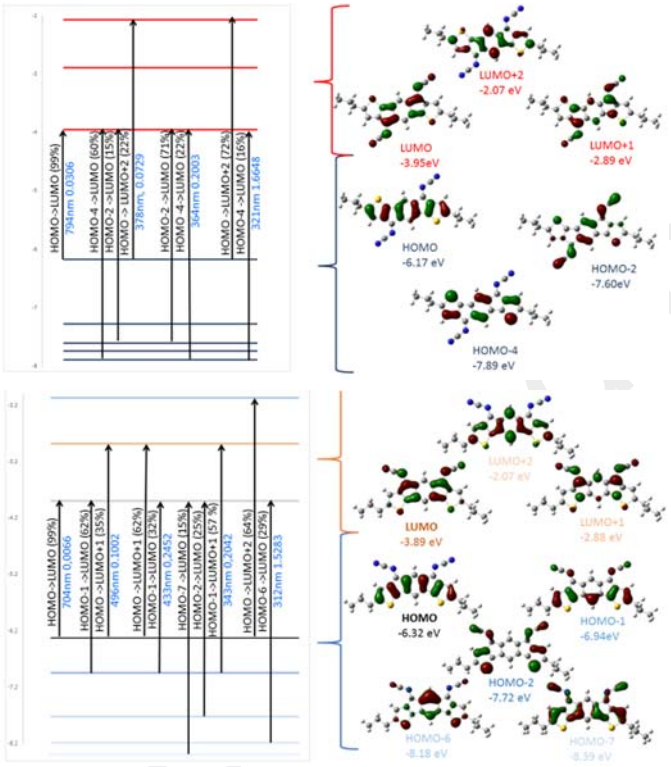

Fig. 10 Representation of the energy levels and the main molecular orbitals obtained by DFT (B3LYP/6-311+G(d,p)) involved in the electronic transitions of ***para*-IDT(=NCN)$_2$** (top) and ***meta*-IDT(=NCN)$_2$** (bottom) obtained by TD-DFT (B3LYP/6-311+G(d,p)) and shown with an isovalue of 0.04 [e bohr^{-3}]$^{1/2}$.

The trend observed for the electrochemical HOMO/LUMO energy levels is in accordance with that obtained from theoretical calculations (Fig. 10 and Table 3).

The HOMO of ***para*-IDT(=NCN)$_2$** (Fig. 10, top) is dispersed on the IDT core with a delocalization over the whole IDT core and the HOMO of ***meta*-IDT(=NCN)$_2$** (Fig. 10, bottom) presents a clear π-conjugation interruption at the two opposite carbon atoms of the central phenyl ring (nodal plane). This difference leads to a deepening of the calculated HOMO energy from the *para*- to the *meta*-isomer (-6.17 eV / -6.32 eV) due to the partial electronic decoupling occurring in the latter. The energy difference between the two HOMO levels (0.15 eV) is similar to that calculated for the two IDT-dicyanovinylene (0.17 eV) confirming that the IDT core is at the origin of this feature and not the bridge functionalization. In contrast the LUMO are mainly localized on the two cyclopentadienyl/cyanoimine cores (Fig. 10) with LUMO energies calculated at -3.95 and -3.89 eV for the *para*- and *meta*-isomer respectively.

Table 3. Selected electronic properties of cyanoimines and dicyanovinylenes IDT derivatives.

	***para*-IDT(=NCN)$_2$**	***para*-IDT(=C(CN)$_2$)$_2$**	***meta*-IDT(=NCN)$_2$**	***meta*-IDT(=C(CN)$_2$)$_2$**
E^{ox}_{peak} / E^{ox}_{onset} (V)[a]	1.46, 1.74 / 1.32	1.44, 1.71, 1.96 / 1.24	1.70 / 1.56	1.60, 2.10 / 1.40
E^{red}_{peak} / E^{red}_{onset} (V)[a]	-0.44, -0.82 / -0.27	-0.41, -0.74, -1.12 / -0.3	-0.44, -0.84 / -0.33	-0.5, -0.89 / -0.33
HOMO (eV)[b]	-5.72	-5.64	-5.96	-5.80
LUMO (eV)[b]	-4.13	-4.10	-4.07	-4.07
ΔE_{el} (eV)[c]	1.59	1.54	1.89	1.73
HOMO (eV)	-6.17	-6.20	-6.32	-6.37
LUMO (eV)	-3.95	-4.21	-3.89	-4.06
ΔE_{theo} (eV)	2.22	1.99	2.43	2.31
ΔE_{opt} (eV)[d]	1.41	1.29	1.61	1.57

[a] *vs* SCE, [b] Calculated from onset oxidation/reduction potential. [c] ΔE_{el} = HOMO-LUMO from electrochemical data. [d] hc/λ = 1239.84/λ (in nm) from absorption spectrum, λ being the low energy absorption band edge.

UV-Vis absorption spectra.

UV-vis absorption spectra recorded in THF are shown in Fig. 11, top.

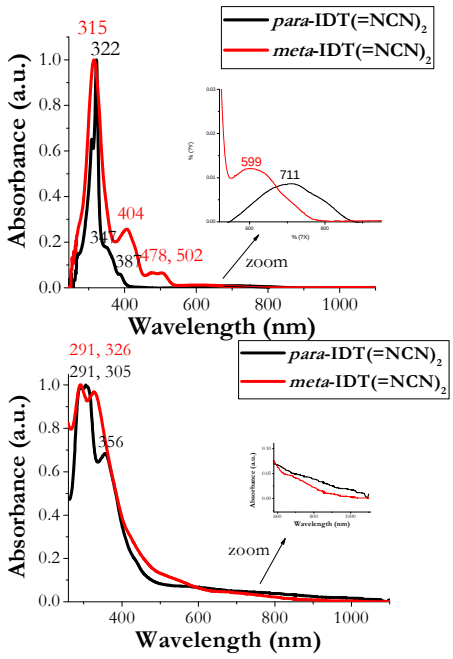

Fig. 11 Absorption spectra of ***para*-IDT(=NCN)$_2$** and ***meta*-IDT(=NCN)$_2$** in THF (top) and in the solid state (bottom, thermally-evaporated thin film, thickness 40 nm). Inset: Focus on the 500-900 nm (top) or 600-1100 nm (bottom) portion of these spectra.

Both compounds present intense and well defined absorption bands between 300 and 550 nm (307, 322, 347(sh), 387 (sh) nm for ***para*-IDT(=NCN)$_2$** and 315, 404, 478, 502 for ***meta*-IDT(=NCN)$_2$**) and very weak absorption bands at lower energy (Inset Fig. 11, maximum recorded at 711 nm for ***para*-IDT(=NCN)$_2$** and at 599 nm for ***meta*-IDT(=NCN)$_2$**). These low energy bands were assigned to a HOMO/LUMO transition possessing a very weak oscillator strength (λ: 793 nm/f:0.0306 for ***para*-IDT(=NCN)$_2$** (Fig. 10, top); λ: 704 nm / f:0.006 for ***meta*-IDT(=NCN)$_2$**) Fig. 10, bottom). The very weak oscillator strengths of this transition can be explained by the absence of significant overlap between the HOMO (located on the IDT core) and the LUMO (located on the cyclopentadienyl-cyanoimine ring). Therefore, this transition presents a strong charge-transfer character. Compared to the HOMO-LUMO transitions recorded for ***para*-IDT(=C(CN)$_2$)$_2$** and ***meta*-IDT(=C(CN)$_2$)$_2$**,[34] these transitions are shifted to lower wavelengths (from 743 to 711 nm in the *para*-series and from 630 to 599 nm in the *meta*-series). The blue shift of ca 30 nm from dicyanovinylenes to cyanoimines is consistent with a shorter π-conjugated pathway in the latters, which is caused by the bridges functionalization. From the onset of these low energy bands, the optical gaps of ***para*-IDT(=NCN)$_2$** and ***meta*-IDT(=NCN)$_2$** were respectively determined at 1.41 eV (λ_{onset}=879 nm) and at 1.61 eV (λ_{onset}= 770 nm) both being shorter than their dicyanovinylenes analogues (1.29 /1.57 eV for ***para*-IDT(=C(CN)$_2$)$_2$** and ***meta*-IDT(=C(CN)$_2$)$_2$**).[34]

In addition, the transition possessing the largest oscillator strength for both isomers (***para*-IDT(=NCN)$_2$**: λ = 321 nm, f = 1.6648 ; ***meta*-IDT(=NCN)$_2$**: λ = 312 nm, f = 1.5283) involves a major contribution of HOMO/LUMO+2 with both molecular orbital located on the IDT core. This calculated transition are in accordance with the more intense absorption bands recorded at 322 nm for ***para*-IDT(=NCN)$_2$** and at 315 nm for ***meta*-IDT(=NCN)$_2$**.

In the solid state (thermally-evaporated thin film possessing a thickness of 40 nm, Fig. 11, bottom), the absorption spectra are red shifted compared to those recorded in solution. The onset absorption band recorded at 1016 nm for ***para*-IDT(=NCN)$_2$** and at 856 nm for ***meta*-IDT(=NCN)$_2$** provides a short ΔE^{opt} of 1.22 and 1.45 eV respectively. The slight ΔE^{opt} contraction from liquid to solid state, around 0.2 eV, results from strong packing in the solid state.

Organic field-effect transistors.

The last important step was to evaluate the impact of the electron-withdrawing N-cyanoimine groups in devices, herein OFETs. Both ***para*- and *meta*-IDT(=NCN)$_2$** have been used as active layer in n-type channel OFETs possessing a bottom-gate bottom-contact (BG-BC) architecture (see device structure in SI). The fabrication process was the following: 150 nm thick aluminium layer was evaporated on a 5 × 5 cm^2 glass substrate and patterned by conventional photolithography. SU-8 2000.5 photoresist from Microchem was then spin coated to obtain a 400 nm thick layer. 50 nm thick gold layer was then thermally evaporated and patterned by photolithography. Finally, the OSCs were deposited by evaporation under vacuum as a 40 nm thick layer. This BG-BC structure in which the OSC is evaporated in the last process step, avoids any structural effect resulting from the following step.

Mobility μ_{FE}, threshold voltage V_{TH}, subthreshold swing SS and the on/off ratio of the drain current (I_{Don}/I_{Doff}) presented I nwere extracted from the transfer characteristics in the linear and saturated regimes of a series of at least five OFETs of different dimensions (W = 4000 µm, L = 3 to 50 µm), fabricated during the same process to get a more precise insight on the reproducibility of the values (see Fig. 12). Table 4 reports the average values and the highest measured linear and saturated mobilities are presented between brackets.

In the first set of measurements, without thermal treatment of the devices after fabrication, one can note that devices using ***para*-IDT(=NCN)$_2$** present better performances than those using ***meta*-IDT(=NCN)$_2$**. The linear/saturated maximum μ_{FE} values strongly increase from 6.7/5.4 ×10^{-5} cm^2 V^{-1}s^{-1} to 0.81/1.4× 10^{-3} cm^2 V^{-1}s^{-1} from ***meta*-IDT(=NCN)$_2$** to ***para*-IDT(=NCN)$_2$**. A similar difference between the two regioisomers has previously been detected in the dicyanovinylene series.[34] For both type of bridges, the ***para*-IDT** core is more efficient when incorporated in OFET than the ***meta*-IDT** core. This feature shows the importance of regioisomerism in the materials design for electronics.

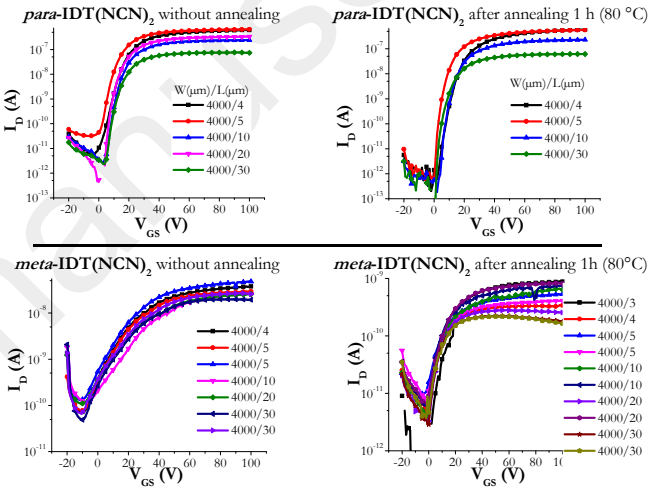

Fig. 12 Transfer characteristics of OFETs with ***para*-IDT(=NCN)$_2$** (Top) and ***meta*-IDT(=NCN)$_2$** (bottom), without annealing (left) or after annealing 1h at 80 °C (right)(V_{DS} = 10 V).

The second set of measurements was performed after annealing the devices at 80 °C during one hour.[34] Again, the linear/saturated maximum μ_{FE} values are also higher for the devices using ***para*-IDT(=NCN)$_2$** compared to those using ***meta*-IDT(=NCN)$_2$** (0.58/1 ×10^{-3} cm^2 V^{-1} s^{-1} *vs* 1.6/2.5×10^{-6} cm^2 V^{-1} s^{-1}, resp.). However, annealing process seems to have two different effects on the devices. The first effect could be related to a better organisation in the insulator/OSC interface. Indeed, subthreshold slopes (SS) were strongly improved in both cases (reaching an interesting value of 1.3 for ***para*-IDT(=NCN)$_2$**) meaning that carrier accumulation in the active channel is favoured with the annealing process. This observation is also strengthened with the improvement of threshold voltage (V_{TH}) (from 14.9 to 13.5 V). Thus, defect density in the first layer of OSC has been decreased.[50] This effect could be linked to an increase of grain size. However, μ_{FE} (generally improved when grain size increases) slightly decreases after annealing treatment. We have to notice that μ_{FE} is extracted from the maximum of transconductance g_m corresponding to a high gate-source voltage V_{GS}. In both cases, drain current I_D

decreased when V_{GS} increased (more easily visible in ***meta*-IDT(=NCN)$_2$**-based OFET). This phenomenon could be linked to a high access resistance in the interface between drain/source and OSC.

Recently, we have shown that the covering of gold drain and source electrodes by self-assembled monolayer (SAM) of DABT (4-(dimethylamino)benzene thiol) can have a beneficial effect on the performance and stability of the resulting OFETs.[34, 82] Devices with gold modified electrodes were fabricated using the same fabrication process as described above. After the thick gold layer was thermally evaporated and patterned by photolithography, the substrates were immersed in a 1.6 mg/mL acetone solution of DABT for 10 min at room temperature under dry-nitrogen atmosphere. Devices were then rinsed with acetone and OSCs were then evaporated in the last process step. Performances are presented in Fig. 13 and summarized in the Table 5.

In a first series of experiments in which the devices were tested without annealing, one can note that for ***para*-IDT(=NCN)$_2$**, the linear/saturated μ_{FE} values are more than doubled compared to the devices without DABT. This is therefore an efficient strategy to strongly increase the device performance. The maximum value, 3.8 × 10^{-3} cm² V^{-1} s^{-1}, remains nevertheless moderate compare to the state of the art.[13-14, 83] Interestingly, this increase of the linear/saturated μ_{FE} values is not observed for ***meta*-IDT(=NCN)$_2$** based devices for which the mobilities remain roughly similar (Table 4) in both type of devices.

A second set of experiments were performed after annealing the devices for 1 hour at 80 °C. Despite a slight increase was observed for saturated μ_{FE} of ***para*-IDT(=NCN)$_2$**, 4.6×10^{-3} cm² V^{-1} s^{-1}, the heating of the devices was deleterious for linear μ_{FE} (Table 5). The same phenomenon observed without DABT could explain this deterioration. Indeed, with DABT, SS is significantly improved (from 3.7 V/dec to 1.4 V/dec for ***para*-IDT(=NCN)$_2$** and from 15.1V/dec to 5.9 V/dec for ***meta*-IDT(=NCN)$_2$**). Channel creation is then improved with the annealing process but μ_{FE} is limited with the dewetting process leading to an increase of access resistance.

As the two compounds possess similar electronic properties, it is clear that the difference in term of performance comes from a different molecular organisation in the bulk of ***meta*-IDT(=NCN)$_2$** rendering the charge transport less efficient than in its isomer ***para*-IDT(=NCN)$_2$**.

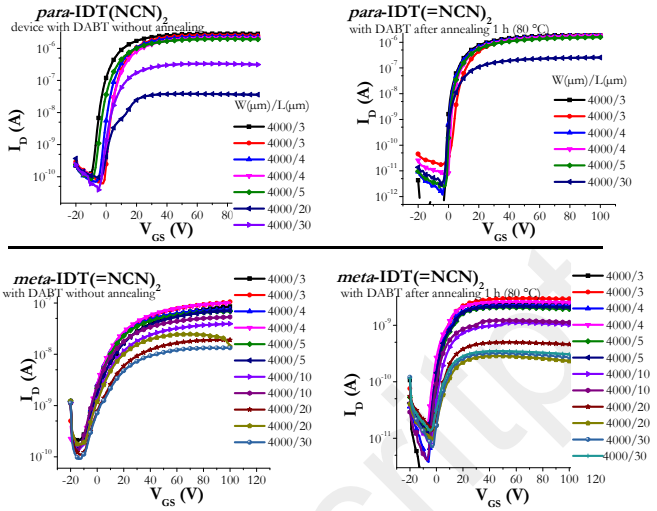

Fig. 13. Transfer characteristics of OFETs with DABT using ***para*-IDT(=NCN)$_2$** (Top) and ***meta*-IDT(=NCN)$_2$** (bottom), without annealing (left) or after annealing 1h at 80 °C (right)(V_{DS} = 10 V).

Then, the annealing process has a positive effect with an increase of the OSC grain size but, because of a too thin layer, dewetting process between grains seems to appear and limits the drain current. This phenomenon has already been observed with C_{60}.[81]As a matter of fact, both isomers self-assemble in the solid state in the same way, namely strips of stacked cores that alternate with cyanoimine groups, and the stacking distance is even equivalent (see above). However, the semiconducting performances of the *para* isomer are certainly enhanced by the superimposition of the cores along stacks, whereas the constraints from the arrangement of lateral groups make that successive *meta*-IDT cores are respectively shifted and turned. It should be mentioned that the introduction of DABT appears to lead to a weaker improvement of the devices performances for ***para*-IDT(=NCN)$_2$** than for previously described ***para*-IDT(=C(CN)$_2$)$_2$**.[34] Tentatively, this is not an effect related to electrode / OSC interface, but from the insulating layer (SU-8/OSC interface). Additional experiments on device optimization and characterization need to be done in order to explain the different performances of the devices. At the present stage, differences of thin film morphology influencing OFET performances could not be checked, but are unlikely due to the identical composition and the similar way of self-assembling.

Table 4. Electrical properties of OFETs

SCO	V_{TH} (V)	V_{ON} (V)	SS (V/dec)	I_{Don}/I_{Doff}	Linear μ_{FE} (μ_{FE} maximum value) (cm² V^{-1} s^{-1})	σ_{lin} (%)	Saturated μ_{FE} (μ_{FE} maximum value) (cm² $V^{-1}s^{-1}$)	σ_{sat} (%)
***para*-IDT(=NCN)$_2$** Without annealing	14.9	0.6	2.5	1.9×10^5	4.3×10^{-4} (8.1×10^{-4})	46.5	9.7×10^{-4} (1.4×10^{-3})	35.1
***para*-IDT(=NCN)$_2$** After annealing at 80°C - 1h	13.5	1.6	1.3	8.8×10^4	3.1×10^{-4} (5.8×10^{-4})	45.2	7.4×10^{-4} (1.0×10^{-3})	36.4
***meta*-IDT(=NCN)$_2$** Without annealing	12.7	-8.4	19.2	3.0×10^2	2.3×10^{-5} (6.7×10^{-5})	83.6	2.4×10^{-5} (5.4×10^{-5})	75
***meta*-IDT(=NCN)$_2$** After annealing at 80°C - 1h	3.7	-0.25	11.7	0.97×10^2	5.3×10^{-7} (1.6×10^{-6})	79.2	9.4×10^{-7} (2.5×10^{-6})	91.5

Table 5. Electrical properties of DABT modified OFETs

SCO	V_{TH} (V)	V_{ON} (V)	SS (V/dec)	I_{Don}/I_{Doff}	Linear μ_{FE} (μ_{FE} maximum value) ($cm^2 V^{-1} s^{-1}$)	σ_{lin} (%)	Saturated μ_{FE} (μ_{FE} maximum value) ($cm^2 V^{-1}s^{-1}$)	σ_{sat} (%)
***para*-IDT(=NCN)$_2$** Without annealing	7.9	-5.1	3.7	4.1×10^5	1.3×10^{-3} (2.1×10^{-3})	37.3	1.9×10^{-3} (3.8×10^{-3})	49.0
***para*-IDT(=NCN)$_2$** After annealing at 80°C - 1h	8.9	-1.4	1.4	5.9×10^4	6.2×10^{-4} (8.4×10^{-4})	31.9	1.7×10^{-3} (4.6×10^{-3})	70.0
***meta*-IDT(=NCN)$_2$** Without annealing	3.1	-12.8	15.1	2.9×10^2	2.2×10^{-5} (4.7×10^{-5})	50.9	3.8×10^{-5} (5.8×10^{-5})	44.7
***meta*-IDT(=NCN)$_2$** After annealing at 80°C - 1h	2.4	-3.1	5.9	4.4×10^2	1.6×10^{-7} (2.2×10^{-6})	27.5	2.1×10^{-6} (3.6×10^{-5})	32.4

Conclusion

In this work, we report the use of electron-withdrawing fragments, namely N-cyanoimines incorporated on the bridges of indacenodithiophene regioisomers. In order to show the impact of the bridge substitution, the main physicochemical properties of these OSCs have been compared to those of their corresponding analogues ***para*-IDT(=C(CN)$_2$)$_2$** and ***meta*-IDT(=C(CN)$_2$)$_2$**, bearing the widely used dicyanovinylene units at their bridges. The four compounds were found to self-organize into lamellar structures, defined by the alternation of layers of conjugated cores and aliphatic tails. The cohesive molecular self-assembling promoted by the dipolar association of cyanoimine or dicyanovinylene groups resulted in the formation of three-dimensional lamellar mesophases that extend from above melting temperature to sample degradation. Compared to dicyanovinylene functionalities, the present cyanoimine groups induce a decrease of the HOMOs energy (from -5.64 eV to -5.72 eV in the *para*-series and from -5.80 to -5.96 eV in the *meta*-series and keep the LUMOs energy almost unaltered (from -4.10 eV to -4.13 eV in the *para*-series and -4.07 eV for both *meta*-derivatives, values from electrochemical measurements). This shows that cyanoimines are very strong electron-withdrawing groups and as good as the famous dicyanovinylene fragments to depress the LUMO energy level of an OSC. This is a key feature in the design of future electron-poor materials. In addition, these fragments are also highly thermally stable, which is a key feature in Organic Electronics. Thanks to their low LUMO levels, both *meta*-IDT(=NCN)$_2$ and *para*-IDT(=NCN)$_2$) have been successfully used as active layer in n-type OFETs using as insulator an organic material, i.e. SU8 insulator and with gold electrodes modified by self-assembled monolayer of DABT. As far as we know, the present work is the second example[76] reported to date of N-cyanoimines based OSC in n-type OFETs.

Herein, higher OFET performances have been obtained. *Para*-IDT(=NCN)$_2$ based devices present higher linear/saturated field-effect mobilities than its regioisomer *meta*-IDT(=NCN)$_2$. As a similar conclusion was drawn for their dicyanovinylenes analogues,[34] the *para*-IDT-core appears to be intrinsically more efficient in OFET than its *meta* isomer, and this finding for the =NCN bridges is explainable by the features of the molecular organization in the solid state. We believe that cyanoimines can present an alternative to widely known electron-withdrawing units such as dicyanovinylene, with induction of comparable semiconducting properties and of considerably improved solubility that facilitates the processing. They deserve to be tested with other π-conjugated systems to fully explore their potential. We are currently working in this direction.

Conflicts of interest

"There are no conflicts to declare".

Acknowledgements

We thanks the Region Bretagne and the Agence de l'Environnement et de la Maîtrise de l'Energie (ADEME) for a studentship (JDP), Dr Bruno Laffite (ADEME), the University of Rennes 1 for financial support (*Action Incitative* 2013), the IETR for financial support, the C.R.M.P.O (Rennes) for mass analysis. This work was granted access to the high performance computing resources of CINES (Montpellier, France) under allocation 2018-A0040805032 awarded by GENCI. BD and BH thank the CNRS and Université de Strasbourg (UNISTRA) for support.

Notes and references

1 J.-H. Jou, S. Kumar, A. Agrawal, T.-H. Li and S. Sahoo, *J. Mater. Chem. C*, 2015, **3**, 2974.
2 *OLED Fundamentals: Materials, Devices, and Processing of Organic Light-Emitting Diodes*, CRC press, 2015.
3 *Organic Light-Emitting Diodes (OLEDs) Materials, Devices and Applications*, Woodhead Publishing, University of Sheffield, UK, 2013.
4 Y. Im, S. Y. Byun, J. H. Kim, D. R. Lee, C. S. Oh, K. S. Yook and J. Y. Lee, *Adv. Funct. Mater.*, 2017, **27**, 1603007.
5 Y. Li, J.-Y. Liu, Y.-D. Zhao and Y.-C. Cao, *Materials Today*, 2017, **20**, 258.

6 C. Poriel and J. Rault - Berthelot, *J. Mater. Chem. C*, 2017, **5**, 3869.
7 M. Romain, S. Thiery, A. Shirinskaya, C. Declairieux, D. Tondelier, B. Geffroy, O. Jeannin, J. Rault-Berthelot, R. Métivier and C. Poriel, *Angew. Chem Int. Ed.*, 2015, **54**, 1176.
8 H. Sasabe and J. Kido, *Eur. J. Org. Chem.*, 2013, 7653.
9 K. S. Yook and J. Y. Lee, *Chem. Rec.*, 2016, **16**, 159.
10 G. Luo, X. Ren, S. Zhang, H. Wu, W. C. H. Choy, Z. He and Y. Cao, *Small*, 2016, **12**, 1547.
11 N. Kaur, M. Singh, D. Pathak, T. Wagner and J. M. Nunzi, *Synth. Met.*, 2014, **190**, 20.
12 *Solar Cells - New Approaches and Reviews*, InTech, 2015
13 X. Gao and Z. Zhao, *Sc. China Chem.*, 2015, **58**, 947.
14 Y. Zhao, Y. Guo and Y. Liu, *Adv. Mater.*, 2013, **25**, 5372.
15 C. Wang, H. Dong, W. Hu, Y. Liu and D. Zhu, *Chem. Rev.*, 2012, **112**, 2208.
16 X. Gao and Y. Hu, *J. Mater. Chem. C*, 2014, **2**, 3099.
17 S. Kola, J. Sinha and H. E. Katz, *J. Polym. Sc. Part B: Pol. Phys.*, 2012, **50**, 1090.
18 K. H. Lee, S. O. Kim, S. Kang, J. Y. Lee, K. S. Yook, J. Y. Lee and S. S. Yoon, *Eur. J. Org. Chem.*, 2012, **2012**, 2748.
19 D. Thirion, C. Poriel, R. Métivier, J. Rault-Berthelot, F. Barrière and O. Jeannin, *Chem. Eur. J.*, 2011, **17**, 10272.
20 D. Thirion, J. Rault-Berthelot, L. Vignau and C. Poriel, *Org. Lett.*, 2011, **13**, 4418.
21 C. Poriel, J. Rault-Berthelot, D. Thirion, F. Barrière and L. Vignau, *Chem. Eur. J.*, 2011, **17**, 14031.
22 M. Romain, D. Tondelier, J.-C. Vanel, B. Geffroy, O. Jeannin, J. Rault-Berthelot, R. Métivier and C. Poriel, *Angew. Chem Int. Ed.*, 2013, **52**, 14147.
23 M. Romain, C. Quinton, D. Tondelier, B. Geffroy, O. Jeannin, J. Rault-Berthelot and C. Poriel, *J. Mater. Chem. C*, 2016, **4**, 1692.
24 C. Poriel, R. Métivier, J. Rault-Berthelot, D. Thirion, F. Barrière and O. Jeannin, *Chem. Commun.*, 2011, **47**, 11703.
25 M. Romain, D. Tondelier, B. Geffroy, O. Jeannin, E. Jacques, J. Rault-Berthelot and C. Poriel, *Chem. Eur. J.*, 2015, **21**, 9426.
26 J. Zhang, B. Zhao, Y. Mi, H. Liu, Z. Guo, G. Bie, W. Wei, C. Gao and Z. An, *Dyes Pigm.*, 2017, **140**, 261.
27 J. Kirkpatrick, C. B. Nielsen, W. Zhang, H. Bronstein, R. S. Ashraf, M. Heeney and I. McCulloch, *Adv. Ener. Mat.*, 2012, **2**, 260.
28 C. Duan, W. Cai, C. Zhong, Y. Li, X. Wang, F. Huang and Y. Cao, *J. Polym. Sc., Part A: Pol. Chem.*, 2011, **49**, 4406.
29 J. Kim, S. H. Kim, I. H. Jung, E. Jeong, Y. Xia, S. Cho, I.-W. Hwang, K. Lee, H. Suh, H.-K. Shim and H. Y. Woo, *J. Mater. Chem.*, 2010, **20**, 1577.
30 Y. Li, M. Gu, Z. Pan, B. Zhang, X. Yang, J. Gu and Y. Chen, *J. Mater. Chem. A*, 2017, **5**, 10798.
31 S. Bebiche, I. Bouhadda, T. Mohammed-Brahim, N. Coulon, J. F. Bergamini, C. Poriel and E. Jacques, *Solid-State Electronics*, 2017, **130**, 49.
32 Y.-I. Park, J. S. Lee, B. J. Kim, B. Kim, J. Lee, D. H. Kim, S.-Y. Oh, J. H. Cho and J.-W. Park, *Chem. Mater.*, 2011, 4038.
33 H. Song, Y. Deng, Y. Gao, Y. Jiang, H. Tian, D. Yan, Y. Geng and F. Wang, *Macromolecules*, 2017, **50**, 2344.
34 J.-D. Peltier, B. Heinrich, B. Donnio, J. Rault-Berthelot, E. Jacques and C. Poriel, *ACS Appl. Mater. Interfaces*, 2017, **9**, 8219.
35 I. Isakov, A. F. Paterson, O. Solomeshch, N. Tessler, Q. Zhang, J. Li, X. Zhang, Z. Fei, M. Heeney and T. D. Anthopoulos, *App. Phys. Lett.*, 2016, **109**, 263301.
36 W. Zhang, J. Smith, S. E. Watkins, R. Gysel, M. McGehee, A. Salleo, J. Kirkpatrick, S. Ashraf, T. Anthopoulos, M. Heeney and I. McCulloch, *J. Am. Chem. Soc.*, 2010, **132**, 11437.
37 M. Romain, M. Chevrier, S. Bebiche, T. Mohammed-Brahim, J. Rault-Berthelot, E. Jacques and C. Poriel, *J. Mater. Chem. C*, 2015, **3**, 5742.
38 L. Sicard, C. Quinton, J.-D. Peltier, D. Tondelier, B. Geffroy, U. Biapo, R. Métivier, O. Jeannin, J. Rault-Berthelot and C. Poriel, *Chem. Eur. J.*, 2017, **23**, 7719.
39 J.-D. Peltier, B. Heinrich, B. Donnio, O. Jeannin, J. Rault-Berthelot and C. Poriel, *Chem. Eur. J.*, 2017, **23**, 17290.
40 A. G. Fix, D. T. Chase and M. M. Haley, *Top. Curr. Chem.*, 2012, **349**, 159.
41 D. Thirion, C. Poriel, F. Barrière, R. Métivier, O. Jeannin and J. Rault-Berthelot, *Org. Lett.*, 2009, **11**, 4794.
42 F. Barrière, C. Poriel and J. Rault-Berthelot, *Electrochim. Acta*, 2013, **110**, 735.
43 C. Poriel, J. Rault-Berthelot and D. Thirion, *J. Org. Chem.*, 2013, **78**, 886.
44 C. K. Frederickson, B. D. Rose and M. M. Haley, *Acc. Chem. Res.*, 2017, **50**, 977.
45 C. Poriel and J. Rault-Berthelot, *Acc. Chem. Res.*, 2018, **51**, 1818.
46 C. Poriel, J.-J. Liang, J. Rault-Berthelot, F. Barrière, N. Cocherel, A. M. Z. Slawin, D. Horhant, M. Virboul, G. Alcaraz, N. Audebrand, L. Vignau, N. Huby, G. Wantz and L. Hirsch, *Chem. Eur. J.*, 2007, **13**, 10055.
47 W. Deuschel, *Helv. Chim. Acta*, 1951, **34**, 168.
48 L. Chardonnens and H. Chardonnens, *Helv. Chim. Acta*, 1958, **41**, 2109.
49 L. Chardonnens and J. Rody, *Helv. Chim. Acta*, 1959, **42**, 1328.
50 S. Bebiche, P. Cisneros-Perez, T. Mohammed-Brahim, M. Harnois, J. Rault-Berthelot, C. Poriel and E. Jacques, *Mater. Chem. Front.*, 2018, **2**, 1631.
51 Z.-P. Fan, X.-Y. Li, .-E. Luo, X. Fei, B. Sun, L.-C. Chen, Z.-F. Shi, C.-L. Sun, X. Shao and H.-L. Zhang, *Adv. Funct. Mater.*, DOI: 10.1002/adfm.201702318, 1702318.
52 T. Nakagawa, D. Kumaki, J.-i. Nishida, S. Tokito and Y. Yamashita, *Chem. Mater.*, 2008, **20**, 2615.
53 M. Ozdemir, D. Choi, G. Kwon, Y. Zorlu, H. Kim, M.-G. Kim, S. Seo, U. Sen, M. Citir, C. Kim and H. Usta, *RSC Adv.*, 2016, **6**, 212.
54 R. Ozdemir, D. Choi, M. Ozdemir, G. Kwon, H. Kim, U. Sen, C. Kim and H. Usta, *J. Mater. Chem. C*, 2017, **5**, 2368.
55 B. J. Kim, Y.-I. Park, H. J. Kim, K. Ahn, D. R. Lee, D. H. Kim, S.-Y. Oh, J.-W. Park and J. H. Cho, *J. Mater. Chem.*, 2012, **22**, 14617.
56 Y. Miyata, T. Minari, T. Nemoto, S. Isoda and K. Komatsu, *Org. Biomol. Chem.*, 2007, **5**, 2592
57 Q. Zhou, P. J. Carroll and T. M. Swager, *J. Org. Chem.*, 1994, **59**, 1294.
58 Y. Li, W. K. Tatum, J. W. Onorato, S. D. Barajas, Y. Y. Yang and C. K. Luscombe, *Polym. Chem.*, 2017, **8**, 5185.
59 W. Jing, Z. Weijing, X. Huan, L. Bin, C. Xiaoping and Z. Haoli, *Chin. J. Chem.*, 2012, **30**, 681.
60 H. Xu, Y. C. Zhou, X. Y. Zhou, K. Liu, L. Y. Cao, Y. Ai, Z. P. Fan and H. L. Zhang, *Adv. Funct. Mater.*, 2014, **24**, 2907.
61 J. Wang, *Appl. Mech. Mater.*, 2013, **331**, 452.
62 H. Tian, Y. Deng, F. Pan, L. Huang, D. Yan, Y. Geng and F. Wang, *J. Mater. Chem.*, 2010, **20**, 7998.
63 C. Zhao, Y. Zhang and M.-K. Ng, *J. Org. Chem.*, 2007, **72**, 6364.
64 Y. Ie, M. Nitani and Y. Aso, *Chem. Lett.*, 2007, **36**, 1326.
65 Y. Ie, Y. Umemoto, M. Nitani and Y. Aso, in *Pure Appl. Chem.*, 2008, vol. 80, p. 589.
66 H. Usta, C. Risko, Z. Wang, H. Huang, M. K. Deliomeroglu, Zhukhovitskiy A., A. Facchetti and T. J. Marks, *J. Am. Chem. Soc.*, 2009, **131**, 5586.

67 H. Usta, A. Facchetti and T. J. Marks, *J. Am. Chem. Soc.*, 2008, **130**, 8580.
68 R. Ozdemir, D. Choi, M. Ozdemir, H. Kim, S. T. Kostakoğlu, M. Erkartal, H. Kim, C. Kim and H. Usta, *ChemPhysChem*, 2017, **18**, 850.
69 W. Frank and R. Gompper, *Tetrahedron Lett.*, 1987, **28**, 3083.
70 A. Aumüller and S. Hünig, *Angew. Chem.*, 1984, **96**, 437.
71 A. S. Batsanov, M. R. Bryce, M. A. Coffin, A. Green, R. E. Hester, J. A. K. Howard, I. K. Lednev, N. Martín, A. J. Moore, J. N. Moore, E. Ortí, L. Sánchez, M. Savirón, P. M. Viruela, R. Viruela and T.-Q. Ye, *Chem. Eur. J.*, 1998, **4**, 2580.
72 D. Schmidt, B. Häupler, C. Friebe, M. D. Hager and U. S. Schubert, *Polymer*, 2015, **68**, 321.
73 P. Sandín, A. Martínez-Grau, L. Sánchez, C. Seoane, R. Pou-Amérigo, E. Ortí and N. Martín, *Org. Lett.*, 2005, **7**, 295.
74 K. Takahashi and K. Kobayashi, *J. Org. Chem.*, 2000, **65**, 2577.
75 K. Kobayashi, Y. Mazaki, H. Namba, K. Kikuchi, K. Saito, I. Ikemoto, S. Hino and N. Kosugi, *J. Mater. Chem.*, 1995, **5**, 1625.
76 S. Chen, Y. Zhao, A. Bolag, J.-i. Nishida, Y. Liu and Y. Yamashita, *ACS Appl. Mater. Interfaces*, 2012, **4**, 3994.
77 K.-T. Wong, T.-C. Chao, L.-C. Chi, Y.-Y. Chu, A. Balaiah, S.-F. Chiu, Y.-H. Liu and Y. Wang, *Org. Lett.*, 2006, **8**, 5033.
78 C. Janiak, *J. Chem. Soc., Dalton Trans.*, 2000, **21**, 3885.
79 A. I. Kitaigorodskii, ed. C. Bureau, New York, 1955.
80 S. Marzouk, A. Khalfallah, B. Heinrich, J. E. Khiari, A. Kriaa and S. Méry, *J. Fluor. Chem.*, 2017, **197**, 15.
81 S. A. Burke, J. M. Topple and P. Grütter, *J. Phys.: Condens. Matter* 2009, **21**, 423101.
82 M. Robin, M. Harnois, Y. Molard and E. Jacques, *Org. Elec.*, 2016, **39**, 214.
83 Q. Meng and W. Hu, *Phys. Chem. Chem. Phys.*, 2012, **14**, 14152.